applied optics

Design of a subwavelength all-metal grating for generating azimuthally polarized beams based on modified particle swarm optimization

Chunlin Zhu,[1,2] Qingbin Jiao,[1] Xin Tan,[1] Wei Wang,[1] and Bayanheshig[1,*]

[1]National Engineering Research Centre For Diffraction Gratings Manufacturing and Application, Changchun Institute of Optics, Fine Mechanics and Physics, Chinese Academy of Sciences, Changchun, Jilin 130033, China
[2]University of Chinese Academy of Sciences, Beijing 100049, China
*Corresponding author: bayin888@sina.com

Received 22 February 2019; revised 21 April 2019; accepted 2 May 2019; posted 2 May 2019 (Doc. ID 360670); published 20 May 2019

A subwavelength metal grating for generating azimuthally polarized beams was designed. The grating material was determined by calculating the total thermal conductivity coefficient. A modified particle swarm optimization (PSO), which has a two-step algorithm structure, and a particle position-determined inertia weight was performed to establish the grating's structural parameters. Results show that an Au–Ti–Cu all-metal structure provides good thermal conductivity. A high duty cycle structure gives the grating high polarization selectivity of approximately 82.63% at 10.6 μm and a minimum of 26.39% in the 9.6–11.6 μm band. The modified PSO is more efficient and requires fewer calculations while maintaining accuracy. The geometrical parameter tolerances were also analyzed. The groove depth fabrication tolerance is 200 nm, and the sidewall angle fabrication tolerance is 19°, which means that the optimized structure is insensitive to structural parameter deviations.

https://doi.org/10.1364/AO.58.004052

1. INTRODUCTION

A subwavelength metal grating for generating azimuthally polarized beams, as the rear mirror in the resonant cavity of a CO_2 laser, can cause the CO_2 laser to output azimuthally polarized beams and improve laser processing efficiency [1–3]. The grating is usually designed to have a concentric rings shape, which can ensure that transverse electric (TE) waves (where the electric field is parallel to the grating ridge) are reflected almost completely, while the transverse magnetic (TM) waves (where the electric field is perpendicular to the grating ridge) are modulated by the grating structure to enable polarization selection. Higher polarization selectivity can cause the azimuthally polarized beam to oscillate within the resonator cavity and will ultimately cause the laser to output an azimuthally polarized beam with high purity [4–6]. Azimuthally polarized beams can be generated using multilayer dielectric film gratings [7], copper gratings [4], and hybrid circular subwavelength gratings [5]. Because of the grating fabrication technology, the depth-to-width ratio of the copper grating is small, which leads to low polarization selectivity. In a hybrid circular subwavelength grating, a layer composed of nanopillars is introduced into the bottom of the groove, and polarization selectivity is improved to 58.63%. However, the nanopillar layer must be generated in a Ge membrane, and this Ge membrane reduces the overall thermal conductivity of the grating. To be adapted for use in high-power laser systems, the grating must be designed using an all-metal structure to increase its thermal conductivity, while high polarization selectivity must be attained by optimizing the structural parameters.

Current design methods for subwavelength metal gratings include the modal method, the transmission matrix method, the inductor–capacitor (LC) circuit model analysis method, and the effective medium theory combined with thin film antireflection design [8–14]. Use of the modal method and effective medium theory can allow the structural parameters of gratings to be obtained by reverse design. However, for gratings with metal substrates, the reverse design method is not applicable because the results are inaccurate. The forward design method of parameter scanning can provide accurate results. However, as the number of parameters, the number of scanning steps, and the range of parameter values increase, the number of calculations required will also increase geometrically, which makes the parametric scanning method slow and inefficient. Particle swarm optimization (PSO) is a robust and stochastic evolutionary strategy that can obtain the desire parameters efficiently. In 2007, Saremi designed guided-mode resonance filters using PSO, and the designed filter's spectrum has good agreement with the target spectrum [15]. In 2015, Tripathy designed a high diffraction efficient holographic grating using PSO [16]. In 2018, Wang designed a compact tunable guided-mode resonant filter with the help of PSO [17]. Also in 2018, Zhang used PSO to optimize the unequal spacing

distribution in an array division multiplexing technique and achieved multi-beam steering with low grating lobes [18].

In this paper, a subwavelength metal grating for generating azimuthally polarized beams with good thermal conductivity and high polarization selectivity was designed. The thermal conductivity coefficients were calculated for gratings composed of different materials, and an all-metal grating structure was selected. A modified PSO algorithm is proposed to solve the problem, since the gratings of these all-metal structures cannot be designed using the reverse method, and parameter scanning is inefficient. Compared with the traditional PSO, this modified PSO algorithm has a higher convergence speed due to its two-step algorithm structure and its particle position-determined inertia weight. The results show that when the material of the grating, the adherent layer, and the substrate is Au–Ti–Cu, and the grating period is 9 μm, the duty cycle is 0.8, and the groove depth is 1.3627 μm, the grating polarization selectivity reaches its optimal value, and the polarization selectivity at the center wavelength then reaches 82.63%. This high duty cycle structure restricts the TM waves, thus reducing TM reflectivity and enlarging the polarization selectivity. The design efficiency is much higher when using PSO than when using the parametric scanning method. The fabrication tolerances of the grating groove depth and the groove sidewall angle are analyzed. The tolerance is large enough to enable grating fabrication.

2. DESIGN METHODS

A. Grating Material Selection

To be able to work in a high-power laser system, the grating must not accumulate much heat. One way is by transmitting unwanted polarized light through a transmission structure, which reduces heat accumulation. Another way is to use a highly conductive material to transfer and dissipate heat rapidly. The transmission multilayer film grating has high requirements for manufacturing equipment. Due to the laboratory conditions, we consider making gratings on a uniform substrate. The substrate materials that are commonly used in grating reflectors include Si, Ge, ZnSe, and Cu. The grating bar material must have high reflectivity in the 9.6–11.6 μm band, and we choose Au here. The substrate must be pre-plated with a layer of Ti before plating with Au to increase layer adhesion. Therefore, four different material combinations are available: Au–Ti–Si, Au–Ti–Ge, Au–Ti–ZnSe, and Au–Ti–Cu. The etching of the Ti layer may bring in new impurities, which may decrease the grating's damage threshold, so it is safer to keep the Ti layer unetched. Since the Ti layer is opaque, the grating will be opaque. For an opaque grating, the thermal conductivity is important. We calculated the total thermal conductivity for each system using the same grating layer and substrate layer thicknesses in each case. The thicknesses of the grating layer and the substrate layer were set at 5 μm and 1 mm, respectively, and the thickness of the intermediate Ti layer required for Au plating was set at 200 nm.

In Table 1, h is the thickness of each layer, H is the total grating thickness, and K is the total thermal conductivity. As shown in the table, the total thermal conductivity of the all-metal structure is relatively high (3.99 W/cm·K), so the Au–Ti–Cu structure is preferred.

Table 1. Total Thermal Conductivity Values of the Gratings

System	H (CM)	K (W/CM·K)
Au–Ti–Si	$h_{Au} + h_{Ti} + h_{Si} = 0.10052$	1.481067
Au–Ti–Ge	$h_{Au} + h_{Ti} + h_{Ge} = 0.10052$	0.601027
Au–Ti–ZnSe	$h_{Au} + h_{Ti} + h_{ZnSe} = 0.10052$	0.180838
Au–Ti–Cu	$h_{Au} + h_{Ti} + h_{Cu} = 0.10052$	3.990995

B. Optimization of Grating Structure Parameters

The structural parameters of the grating affect its polarization performance, and it is necessary to adjust the grating structure parameters to make its optical performance conform to the design objectives. The structure of the grating is shown in Fig. 1. The grating has a concentric rings shape. As a laser cavity mirror, light is normally incident on the grating. The grating works in the 9.6–11.6 μm band, and high polarization selectivity is required at the central wavelength. Since the local reflectivity of the grating has an effect on the output laser [7], a high polarization selectivity is good for the quality of the output laser. At 10.6 μm, TE waves should have high reflectivity, and TM waves should have low reflectivity. At 9.6 and 11.6 μm, the difference between the reflectivities of the TE and TM waves is generally required to be no less than 5% [4]. To improve its energy utilization, the grating is designed using a subwavelength structure, i.e., the grating period is no more than 9.6 μm. According to the effective medium theory, the subwavelength metal grating is equivalent to a metal film layer for the incident TE wave, which can be almost totally reflected. TE wave reflectivity has little relation to the structural parameters of the grating (e.g., its period, groove depth, or duty cycle). For TM waves, the grating is equivalent to a dielectric film layer, and the structural parameters of the grating will thus modulate the TM wave reflectivity [12,19]. Therefore, the TM wave reflectivity should be designed to be as low as possible in the 9.6–11.6 μm range. Considering that the optimization results may not be in accord with the desired reflectivity perfectly, it is good to set a higher optimization target, which means that the difference between TE and TM reflectivity should be large, so the target reflectivity at 10.6 μm is set to be 0%. The difference between the TE and TM wave reflectivities at 9.6 and 11.6 μm should be greater than 5%. Because of the inevitable grating surface roughness produced by the fabrication processes, the TE wave reflectivity cannot reach 100%; the reflectivity of the TM waves at 9.6 and 11.6 μm is designed to be no more than 80%.

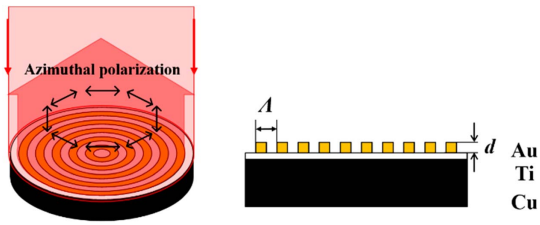

Fig. 1. Subwavelength all-metal grating for generating azimuthally polarized beams.

PSO, which was proposed by Kennedy and Eberhart in 1995 [20,21], can be used to calculate the diffraction efficiencies of multiple wavelengths simultaneously when using the same group of grating structure parameters. By investigating the degree of matching between the designed diffraction efficiency curve and the target diffraction efficiency curve, an optimized structure can be achieved [22–24].

PSO is used to optimize the grating structure parameters, and the basic PSO flow is shown in Fig. 2. The algorithm is divided into two steps: first, the "search for approximate optimum using the central wavelength" is used and then the "search for the exact optimum by multi-wavelength matching". In the first step, the grating structural parameters that achieve the lowest TM reflectivity at 10.6 μm are obtained. This group of structural parameters is then substituted into the second step to act as the "inducing" particle, the structural parameters are then optimized until the TM reflectivity of the grating is the lowest in the 9.6–11.6 μm band, and the results are regarded as the optimal structural parameters. In both steps, the number of particles N is selected to be seven. Each particle's position is a vector that represents the particle parameters (period Λ, groove depth d, and duty cycle DC). The velocity of the particle represents the change in the particle's position in each design iteration. Because of the fabrication capacity, the ranges of Λ, d, and DC were respectively set at 3–9 μm, 0–5 μm, and 0.1–0.8. The maximum velocities were 6 μm, 5 μm, and 0.7, respectively.

First, the position $X(\Lambda, d, \mathrm{DC})$ and velocity $V(\delta\Lambda, \delta d, \delta\mathrm{DC})$ parameters of the particles are randomly generated. The fitness FF1 of each particle is then calculated via a rigorous coupled wave analysis (RCWA). The best personal fitness P_{best} and the best global fitness G_{best} among all the particles contained in each iteration are recorded. Using P_{best} and G_{best}, the change velocity of the particle position is determined, and the particle position is then iterated. The iteration stops when G_{best} meets its termination condition, and the position vector corresponding to G_{best} is the approximate optimal parameter.

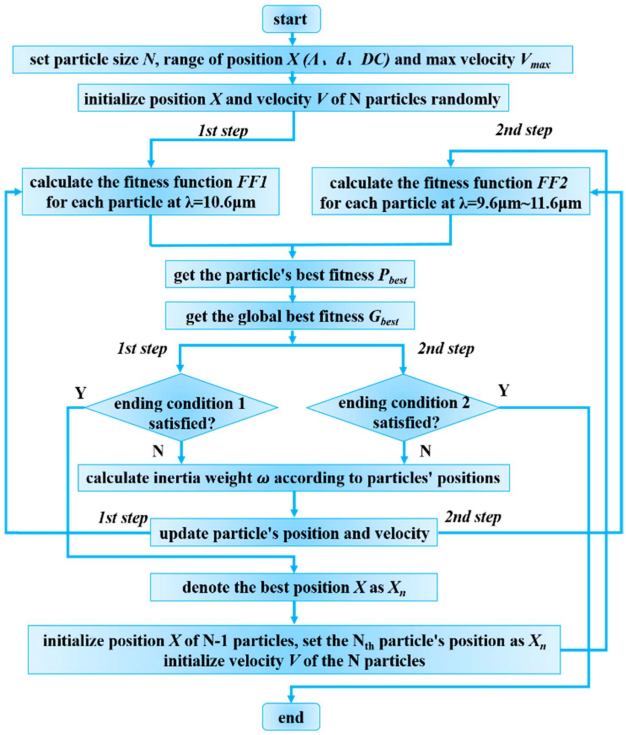

Fig. 2. Flowchart for modified PSO algorithm.

In the first step, for each particle, the fitness function is the TM wave reflectivity calculated using Λ, d, and DC at 10.6 μm as follows:

$$\mathrm{FF1} = R_{\mathrm{design}}. \tag{1}$$

Position updating represents an important step in the iterative process. The position update equation for a particle i is given as follows:

$$\begin{aligned} X_i^{k+1} &= X_i^k + V_i^k, \\ V_i^{k+1} &= \omega \cdot V_i^k + c_1 \cdot \mathrm{rand} \cdot (P_{\mathrm{best}}X_i - X_i^k) \\ &\quad + c_2 \cdot \mathrm{rand} \cdot (G_{\mathrm{best}}X - X_i^k). \end{aligned} \tag{2}$$

ω, c_1, and c_2 are weight factors. V_i^k is the speed of particle i in iteration k. $P_{\mathrm{best}}X_i$ is the position vector that corresponds to the particle's historical best fitness $P_{\mathrm{best\,i}}$. X_i^k is the particle's position vector in iteration k. $G_{\mathrm{best}}X$ is the position vector that corresponds to the best global fitness G_{best}, and rand is a random number that is generated within the uniformly distributed probability between 0 and 1.

ω, c_1, and c_2 are used to limit the effects of the individual inertia velocity, the optimal particle position, and the optimal position of the population on the particle velocity. c_1 and c_2 are set at 0.5 and 2, respectively.

The inertial weight factor modulated by the particle position is given by

$$\omega = \omega_0 \times \sqrt{\left(\frac{G_{\mathrm{best}}X - X_{\mathrm{i}}}{(X_{\max} - X_{\min})/2}\right)^2}. \tag{3}$$

Here, $\omega_0 = 1.2$ is the initial inertial weight factor, while $X_{\max}$ and $X_{\min}$ are the upper and lower boundaries of the particle position, respectively. Shi pointed out that when the inertia weight is large, the global exploration ability of the algorithm is strong, and, when the inertia weight is small, the local exploration ability of the algorithm is strong. Since it is good for the algorithm to have a strong ability of global exploration at the beginning and have a strong ability of local exploration at the end, the strategy of gradually reducing the inertial weight is preferred [25]. Shi proposed that the inertial weight should reduce linearly based on the number of iterations [26]:

$$\omega = \omega_0 \times \left(1 - \frac{k}{\mathrm{Maxnum}}\right). \tag{4}$$

In this strategy, only when k is nearly equal to Maxnum, can ω become small enough and enhace the local exploration ability. However, when the termination condition is a certain threshold, the number of iterations k is usually much smaller than Maxnum, which makes the decrease of ω not obvious, and the algorithm performance is affected. The inertial weight calculation method we propose here [Eq. (3)] is based on the position of the particle: when the particle is gradually close to the optimal solution, ω is significantly reduced, and the local

exploration ability is enhanced. Redundant exploration is avoided, and the performance of the algorithm is improved. Compared with the calculation method based on the number of iterations, the new method can improve the convergence speed.

The ending condition of the iteration process is set at 0.16, which is empirical data obtained from our previous experiments. This ending condition can reduce the number of iterations without losing accuracy. Additionally, Maxnum = 200 is set as the maximum number of iterations to ensure that the algorithm would not get into an endless loop when an error occurs.

The approximate optimal structure parameters are determined in the first step, and these parameters are then added to the second step to act as a set of initial values. Due to the guiding effect of the optimal structural parameters obtained in the first step, the optimization efficiency of the second step is greatly improved. In the second step, the fitness function is defined as the fitness of the target curve and the design curve for the TM wave's reflectance:

$$\mathrm{FF2} = \sqrt{\frac{\sum_{i=1}^{M} (R^i_{\mathrm{object}} - R^i_{\mathrm{design}})^2}{M}}. \tag{5}$$

Here, $M = 5$, which is the number of selected wavelengths in the 9.6–11.6 μm range. R^i_{object} is the object reflectivity, and R^i_{design} is the designed reflectivity. The ending condition for the second step is $G_{\mathrm{best}} < 0.449$, and the maximum number of iterations is Maxnum = 200. Empirical data obtained from our previous experiments is also 0.449, which can reduce the number of iterations without losing accuracy and ensure that the optimized structural parameters meet the design requirements.

3. RESULTS AND DISCUSSION

A. Calculation Results

The optimal structure produced by the PSO is denoted by the parameters $\Lambda = 9$ μm, $d = 1.3627$ μm, and DC = 0.8. The design results show that both the period and the duty cycle reach the maxima of their value ranges, which indicates that if there are no limits to these value ranges, a larger period and a higher duty cycle would be likely to be closer to the optimal results. However, because of the fabrication restrictions, it is risky to increase the period and the duty cycle further. Because these results have already satisfied the design objectives, the current design results are acceptable.

The reflectivity characteristics of the designed grating are shown in Fig. 3.

The designed structure has a TM wave reflectivity of approximately 71.61% at 9.6 μm and 57.63% at 11.6 μm. At 10.6 μm, the TM wave reflectivity is 15.37%. The TE wave reflectivity is always approximately 98% in the 9–12 μm band, so the polarization selectivity of the grating is no less than 26.39% in the 9.6–11.6 μm band and is approximately 82.63% at 10.6 μm. Finite-difference time-domain (FDTD) analysis was used to simulate the reflection field of the grating at 10.6 μm. The electric vector distributions are shown in Fig. 4.

The figure shows that the electric vector is distributed over a ring shape, and the TE wave reflectivity is close to 1, while the

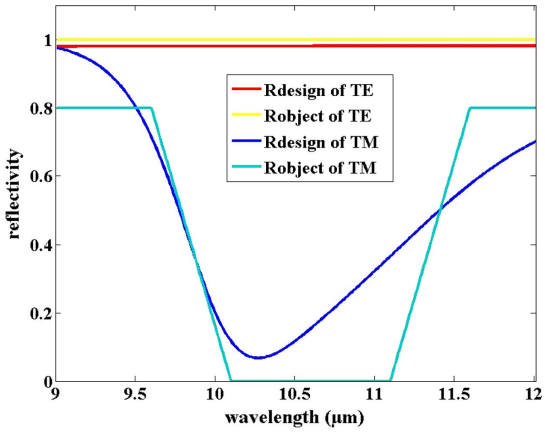

Fig. 3. Optimized polarization performance of grating structure.

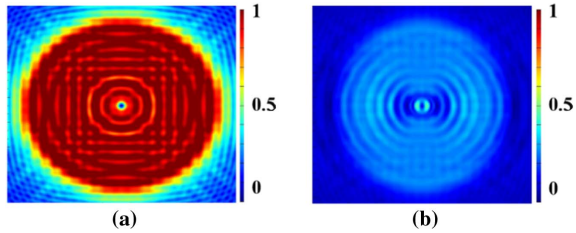

Fig. 4. Reflecting electric vector distributions [(a) TE waves; (b) TM waves].

TM wave reflectivity is very low, thus indicating that the grating reflection produces azimuthally polarized light and offers high polarization selectivity.

To analyze the polarization mechanism, the electromagnetic field distribution in the grating region at 10.6 μm is simulated, with results as shown in Fig. 5.

The figure shows that the TE polarization is reflected almost completely at the top of the grating ridge, while most of the energy of the TM wave is confined within the grating groove. In the grating groove, most of this energy is constrained to the metal–dielectric interface because of the coupling behavior of the surface plasmon polariton (SPP) modes. The coupling of the SPP modes between the two interfaces causes the energy to be constrained between the two side walls. The grating groove and the grating ridge trap and absorb the TM energy, resulting in a reduction of the TM reflectivity. When the duty cycle becomes lower, the dilated grooves lose the ability to trap the TM field, and the reflectivity thus increases, as shown in Figs. 5(c) and 5(d).

B. Algorithm Efficiency

When the ending condition of the PSO is set to reach the maximum number of iterations (i.e., MaxNum = 200), the change in the optimal fitness with increasing numbers of iterations is as shown in Fig. 6.

The algorithm converges to the optimal value after approximately 20 iterations, indicating that the algorithm has a fast convergence rate. Among the various steps of the algorithm,

calling the RCWA to calculate the diffraction efficiency (R_{design}) is the most time-consuming step. The number of times RCWA is called determines the efficiency of the algorithm. In the parameter scanning method, only three wavelengths (9.6, 10.6, and 11.6 μm) are selected, and the scanning steps of Λ, d, and DC are set to 1 μm, 0.01 μm, and 0.1, respectively. The RCWA call number is then enlarged to $3 \times 7 \times 500 \times 8 = 84,000$ times. In the PSO, the total number of calls is the product of the numbers of particles, wavelengths, and iteration times, i.e., $7 \times 1 \times 200 + 7 \times 5 \times 200 = 8400$ times, which is a far smaller number than that obtained for the parametric scanning method. In addition, Fig. 6 shows that if the ending condition of the algorithm is set at an appropriate threshold, the number of iterations required will be reduced significantly, thus further improving the computational efficiency.

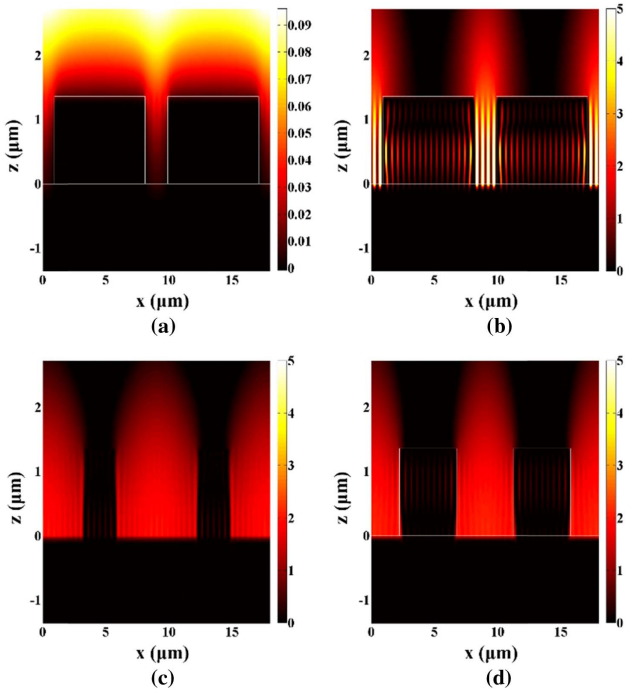

Fig. 5. Electromagnetic field distributions at $\lambda = 10.6$ μm. (a) Ey (10^4 V/m) distribution of the TE wave. (b) Hy (A/m) distribution of the TM wave (DC = 0.8). (c) Hy (A/m) distribution of the TM wave (DC = 0.3). (d) Hy (A/m) distribution of the TM wave (DC = 0.5).

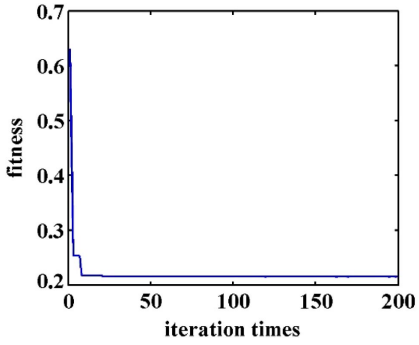

Fig. 6. Schematic diagram showing algorithm convergence.

C. Fabrication Tolerance

The grating was fabricated using the methods of photolithography and electrodeposition. First, the photoresist grating was formed on the metal substrate, and then Au was deposited on the photoresist grating. Finally, the photoresist was dissolved using acetone. The period and the duty cycle of the grating are determined by the exposure mask, and the fabrication accuracy of this mask is 5 nm. The grating's structural errors mainly occur in the sidewall angle of the groove and the height of the grating ridge.

1. Sidewall Angle

During fabrication of the photoresist gratings, the sidewalls of the grating ridges do not usually remain completely steep. When the sidewall has an inclination angle, the upper surface of the metal ridge fabricated by electrodeposition will be broadened to become an inverted trapezoid, as shown in Fig. 7.

The influence of the sidewall angle of the metal grating ridges on the reflectivity is shown in Fig. 8.

As the sidewall angle gradually increases, the TM reflectivity for each wavelength changes in a periodic-like manner and shows an overall upward trend. At approximately 11°, the reflectivity drops at all wavelengths, which means that when the sidewall angle changes, the TM modulation does not always become worse, and an angle of the appropriate size can even increase the polarization selectivity. When the sidewall angle increases to 20°, the TM reflectivity at 9.6 μm exceeds 80%, while in the range from 1° to 19°, the TM reflectivity for all wavelengths does not exceed 80%. We simulated the electromagnetic field distributions of the TM waves at 10.6 μm for different sidewall angles, as shown in Fig. 9.

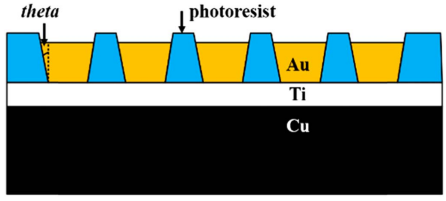

Fig. 7. Metal ridges deposited in the photoresist mask are inverted trapezoid shapes.

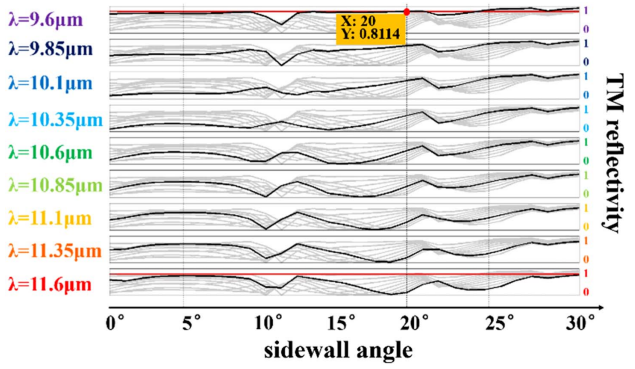

Fig. 8. Black lines: TM wave reflectivity at different wavelengths. Grey lines: general tendencies of reflectivity at nine wavelengths. Red lines: reflectivity = 0.8.

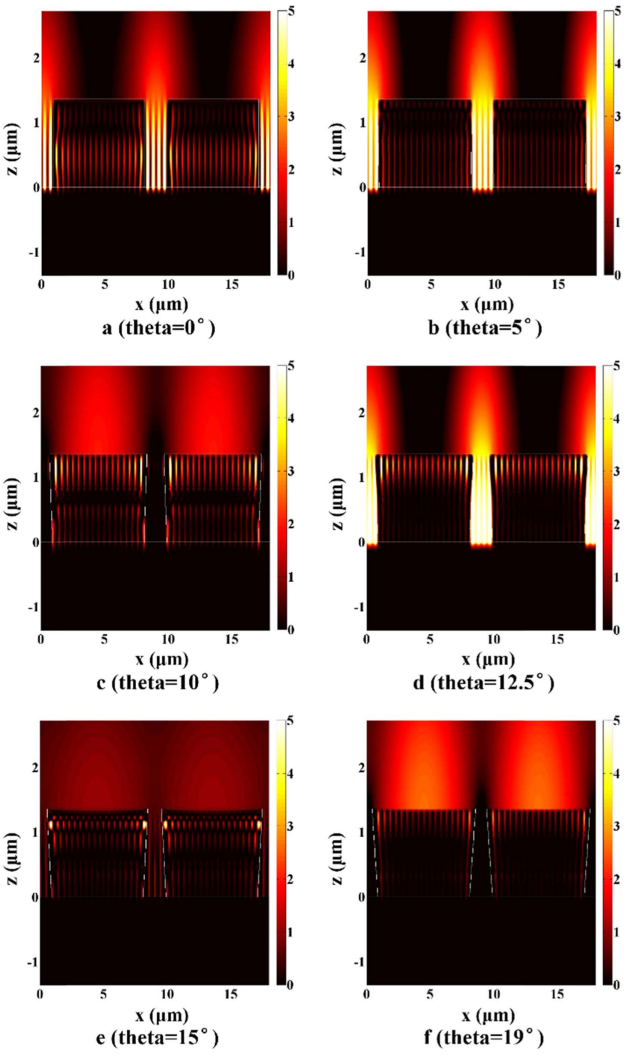

Fig. 9. TM change in mode field strength Hy (A/m) with sidewall angle at $\lambda = 10.6$ μm.

The electromagnetic field distribution shows that when theta is 0°, 5°, and 12.5°, the TM waves are mainly constricted within the grating grooves and thus the reflectivity decreases. Compared with the sidewall angle of 0°, when theta has values of 5° and 12.5°, the reduction in the groove wall symmetry leads to an energy leakage, and thus the TM reflectivity is higher than that at 0°. In Figs. 9c and 9e, it can be seen that the TM wave is largely absorbed by the two top angles of the grating ridges. Because there is nearly zero TM leakage, the reflectivity is extremely small. When the angle is 10°, the top surface of the grating ridge will reflect the energy, but this proportion of the energy is small when compared with the energy leakage shown in Figs. 9b and 9d. When the sidewall angle increases to 19°, the groove width is too small, which means that the grating nearly becomes a flat metal plate layer, and thus the grooves' ability to restrict the TM waves declines. Even at angles of around 22°–24°, where the curves shown in Fig. 8 fall again, the TM reflectivity will never reach a significant minimum, so the sidewall angle should be kept within 19° during fabrication.

2. Groove Depth

During Au deposition, the height of the Au ridge, i.e., the grating groove depth, should be controlled precisely. The TM reflectivity of the grating at the different groove depths is shown in Fig. 10.

As shown in Fig. 11, when the groove depth increases gradually, the valley value of the TM reflectivity moves gradually towards the long wave direction, which indicates that an increase in the groove depth will cause TM reflectivity to increase gradually at the short wave end (9.6 μm) while gradually decreasing at the long wave end (11.6 μm). When the groove depth is small, it is easier for the TM waves to meet the restriction at 9.6 μm, while it is not easy for these waves to meet the restriction at 11.6 μm. As the groove depth increases, the TM reflectivity also increases at 9.6 μm but decreases at 11.6 μm. We can thus determine the tolerance by considering the reflectivity changes with groove depth at 9.6 and 11.6 μm.

When the incident wavelength is 9.6 μm, the groove depth that satisfies the condition when the TM's reflectivity is less than 80% ranges from 0.64 to 1.43 μm. When the incident wavelength is 11.6 μm, the groove depth ranges from 1.23 to 2.31 μm. Therefore, the acceptable height ranges from 1.23 to 1.43 μm, and the tolerance is thus approximately 200 nm. The depositing rate of B&P Limited's Au electrodeposition technology is 1.2 μm/10 min [27]. Under this depositing rate, a 200 nm tolerance means that we have as much as 100 s to control the deposition. The character of photoresist

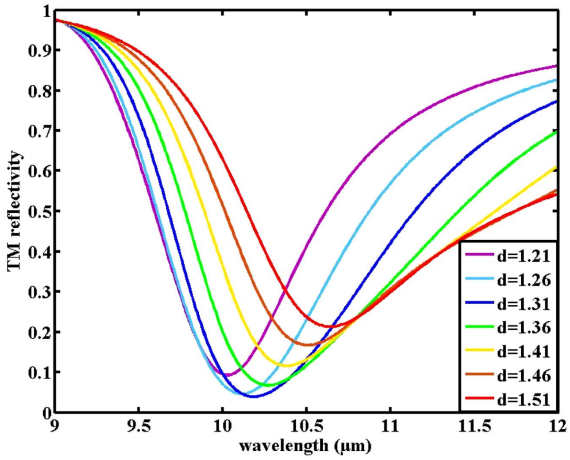

Fig. 10. Reflectivity at various groove depths.

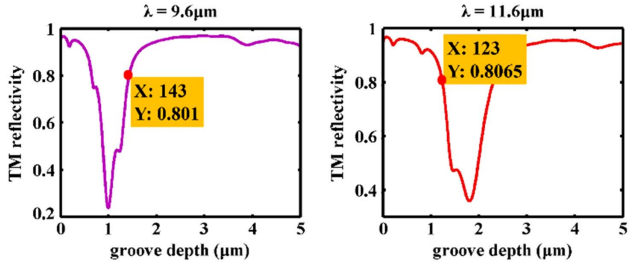

Fig. 11. Groove depth allowance fields at $\lambda = 9.6$ μm and $\lambda = 11.6$ μm.

determines the exposure-development resolution. Using SU-8 photoresist from MicroChem Corp., the photoresist grating has a nearly vertical sidewall [28]; hence, a 19° tolerance is enough for the photoresist grating's fabrication.

4. CONCLUSION

A subwavelength all-metal grating for generating azimuthally polarized beams with high thermal conductivity and high polarization selectivity is designed in this work. The Au–Ti–Cu all-metal structure was determined by calculating the total thermal conductivity of the grating using different material systems. A modified PSO is proposed and used to optimize the grating's structural parameters. The grating structure obtained (period $\Lambda = 9$ μm, groove depth $d = 1.3627$ μm, and duty cycle $DC = 0.8$) has high polarization selectivity in the 9.6–11.6 μm band. The difference between the reflectivities of the TE and TM polarizations is more than 26.39% over this band and is approximately 82.63% at the central wavelength of 10.6 μm. The high duty cycle structure and the relatively large depth/width groove cause the TM electromagnetic field to be constrained within the grating's grooves, and the energy is then absorbed by the grating ridges, thus meaning that the TM reflectivity is small. With the TE wave being almost totally reflected, the polarization selectivity is enhanced. When compared with the parametric scanning method, PSO can not only ensure the accuracy of the design, but can also greatly reduce the number of times that RCWA must be performed, thus improving the design efficiency. Based on an analysis of the tolerance, the sidewall angle should be limited to within 19° during fabrication, and the groove depth fabrication tolerance is 200 nm. These relatively large tolerances reduce the difficulty of grating fabrication.

Funding. Ministry of Science and Technology of the People's Republic of China (MOST); National Key Scientific Instrument and Equipment Development Project of China (61227901).

REFERENCES

1. V. G. Niziev and A. V. Nesterov, "Influence of beam polarization on laser cutting efficiency," J. Phys. D **32**, 1455–1461 (1999).
2. R. Weber, A. Michalowski, M. A. Ahmed, V. Onuseit, V. Rominger, M. Kraus, and T. Graf, "Effects of radial and tangential polarization in laser material processing," Phys. Procedia **12**, 21–30 (2011).
3. M. Meier, V. Romano, and T. Feurer, "Material processing with pulsed radially and azimuthally polarized laser radiation," Appl. Phys. A **86**, 329–334 (2007).
4. V. G. Niziev, V. P. Yakunin, and N. G. Turkin, "Generation of polarization-nonuniform modes in a high-power CO_2 laser," Quantum Electron **39**, 505–514 (2009).
5. Z. Jiang, L. Bo, Z. Heng, W. Wenjin, H. Yi, L. Sisi, and W. Youqing, "Generation of azimuthally polarized beams in fast axial flow CO_2 laser with hybrid circular subwavelength grating mirror," Appl. Opt. **53**, 3706–3711 (2014).
6. K. M. Thomas, T. Svetlen, A. V. Tishchenko, G. Deyan, and P. Olivier, "Azimuthally polarized laser mode generation by multilayer mirror with wideband grating-induced TM leakage in the TE stopband," Opt. Express **20**, 5392–5401 (2012).
7. R. Martin, H. Matthias, S. Thomas, P. Christof, V. Andreas, and O. Wolfgang, "Circular grating waveguide structures for intracavity generation of azimuthal polarization in a thin-disk laser," Opt. Lett. **37**, 1763–1765 (2012).
8. R. Brauer and O. Bryngdahl, "Design of antireflection gratings with approximate and rigorous methods," Appl. Opt. **33**, 7875–7882 (1994).
9. H. Cory and C. Zach, "Wave propagation in metamaterial multilayered structures," Microwave Opt. Technol. Lett. **40**, 460–465 (2010).
10. Z. M. Zhang and C. J. Fu, "Unusual photon tunneling in the presence of a layer with a negative refractive index," Appl. Phys. Lett. **80**, 1097–1099 (2002).
11. J. B. Pendry, "Photonic band structures," Mod. Opt. **41**, 209–229 (1994).
12. I. Richter, P. C. Sun, F. Xu, and Y. Fainman, "Design considerations of form birefringent microstructures," Appl. Opt. **34**, 2421–2429 (1995).
13. B. W. Shore, M. D. Perry, J. A. Britten, R. D. Boyd, M. D. Feit, H. T. Nguyen, R. Chow, G. E. Loomis, and L. Lifeng, "Design of high-efficiency dielectric reflection gratings," J. Opt. Soc. Am. A **14**, 1124–1135 (1997).
14. B. J. Lee, L. P. Wang, and Z. M. Zhang, "Coherent thermal emission by excitation of magnetic polaritons," Opt. Express **16**, 11328–11336 (2008).
15. M. S. Saremi and R. Magnusson, "Particle swarm optimization and its application to the design of diffraction grating filters," Opt. Lett. **32**, 894–896 (2007).
16. A. K. Tripathy, S. K. Das, M. Sundaray, and S. K. Tripathy, "Particle swarm optimization for the design of high diffraction efficient holographic grating," Am. J. Com. Sci. Eng. Sur. **3**, 28–33 (2015).
17. D. Y. Wang and Q. K. Wang, "Particle swarm optimization and its application to the design of a compact tunable guided-mode resonant filter," Chin. Phys. B. **27**, 037801 (2018).
18. B. Zhang, Y. Liu, Z. Q. Zhao, and P. Yan, "Multi-beam steering with low grating lobes using optimized unequally spaced phased array," Opt. Commun. **427**, 48–53 (2018).
19. W. Guo, Z. Li, H. Gao, L. Xia, L. Shi, Q. Deng, and C. Du, "Design of infrared polarizer based on sub-wavelength metal wire grid," Proc. SPIE **8759**, 87593I (2013).
20. J. Kennedy and R. C. Eberhart, "Particle swarm optimization," in *Proceedings of IEEE International Conference on Neural Networks*, Perth, Australia (1995), pp. 1942–1948.
21. R. C. Eberhart and J. Kennedy, "A new optimizer using particle swarm theory," in *Proceedings of the Sixth International Symposium on Micro Machine and Human Science*, Nagoya, Japan (1995).
22. Y. Liu, Z. Yu, H. Yang, N. Zhang, Q. Feng, and X. Zhang, "Numerical optimization and simulation to wavelength-division multiplexing isolation filter consisted of two identical long period fiber grating," Opt. Commun. **246**, 367–372 (2005).
23. D. K. Le, Q. T. Tran, S. Lee, and S. Kim, "Ultra broadband absorption of SPPs enhanced dual grating thin film CIGS solar cell enabled by particle swarm optimization," J. Opt. Soc. Korea **18**, 429–435 (2014).
24. S. S. Mehrdad and M. Robert, "Particle swarm optimization and its application to the design of diffraction grating filters," Opt. Lett. **32**, 894–896 (2007).
25. Y. H. Shi and R. C. Eberhart, "Parameter selection in particle swarm optimization," in *Proceedings of the Annual Conference on Evolutionary Programming* (1998), pp. 591–600
26. Y. H. Shi and R. C. Eberhart, "A modified particle swarm optimizer," in *Proceedings of IEEE Conference on Computational Intelligence* (IEEE, 1998), pp. 69–73.
27. B&P Limited., "Process parameters of Au electrodepsition," http://www.bandphk.com/e%e9%9b%bb%e9%91%84%e7%b3%bb%e5%88%97%e8%a4%87%e6%9c%ac.html.
28. MicroChem Corp., "NANOTM SU-8 negative tone photoresist formulations," http://www.microchem.com/pdf/SU8_2-25.pdf.